

Accepted manuscript

Fei, H., Liu, Z., McCammon, C., Katsura, T.

**Oxygen vacancy substitution linked to ferric iron in bridgmanite at 27
GPa.**

***Geophysical Research Letters*, Volume 47, Issue 6, e2019GL086296, 2020.**

<https://doi.org/10.1029/2019GL086296>

Received 19 NOV 2019

Accepted 1 MAR 2020

Accepted article online 5 MAR 20

Oxygen vacancy substitution linked to ferric iron in bridgmanite at 27 GPa

Hongzhan Fei*, Zhaodong Liu, Catherine McCammon, Tomoo Katsura

Bayerisches Geoinstitut, University of Bayreuth, Bayreuth D95440, Germany

*H. Fei (hongzhan.fe@uni-bayreuth.de)

Abstract:

Ferric iron can be incorporated into the crystal structure of bridgmanite by either oxygen vacancy substitution ($\text{MgFeO}_{2.5}$ component) or charge-coupled substitution (FeFeO_3 component) mechanisms. We investigated the concentrations of $\text{MgFeO}_{2.5}$ and FeFeO_3 in bridgmanite in the $\text{MgO-SiO}_2\text{-Fe}_2\text{O}_3$ system at 27 GPa and 1700-2300 K using a multi-anvil apparatus. The FeFeO_3 content increases from 1.6 to 7.6 mol% and from 5.7 to 17.9 mol% with and without coexistence of $(\text{Mg,Fe})\text{O}$, respectively, with increasing temperature from 1700 to 2300 K. In contrast, the $\text{MgFeO}_{2.5}$ content does not show clear temperature dependence, i.e., $\sim 2\text{-}3$ mol% and < 2 mol% with and without coexistence of $(\text{Mg,Fe})\text{O}$, respectively. Therefore, presence of $(\text{Mg,Fe})\text{O}$ enhances the oxygen vacancy substitution for Fe^{3+} in bridgmanite. It is predicted that Fe^{3+} is predominantly substituted following the oxygen vacancy mechanism in $(\text{Mg,Fe})\text{O}$ -saturated Al-free bridgmanite when Fe^{3+} is below ~ 0.025 pfu, whereas the charge-coupled mechanism occurs when $\text{Fe}^{3+} > 0.025$ pfu.

Plain language summary:

Bridgmanite, the most abundant mineral of the Earth's lower mantle, can contain Fe^{3+} although the valence of iron is 2+ in general. An important question is how Fe^{3+} is substituted in the crystal structure of bridgmanite. It may form the $\text{MgFeO}_{2.5}$ component, in which oxygen anions are partly missing. Or it may form the FeFeO_3 component, which has no missing cations or anions. Since bridgmanite is present in the lower mantle together with $(\text{Mg,Fe})\text{O}$, we investigated the $\text{MgFeO}_{2.5}$ and FeFeO_3 contents in Al-free bridgmanite that coexists with and without $(\text{Mg,Fe})\text{O}$ under the topmost lower mantle conditions. The results show that the presence of $(\text{Mg,Fe})\text{O}$ enhances the formation of $\text{MgFeO}_{2.5}$. The solubility of $\text{MgFeO}_{2.5}$ component is about 2.5 mol% in bridgmanite that coexists with $(\text{Mg,Fe})\text{O}$, whereas it is nearly zero when $(\text{Mg,Fe})\text{O}$ is absent.

Keywords:

bridgmanite; ferric iron; oxygen vacancy substitution; charge-coupled substitution; lower mantle

Key points:

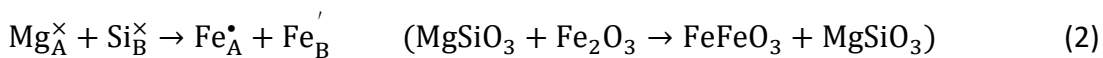
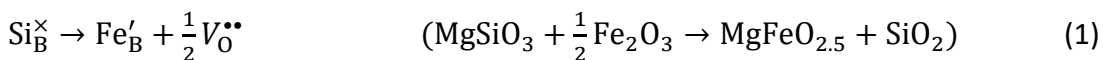
The presence of $(\text{Mg,Fe})\text{O}$ enhances the formation of the $\text{MgFeO}_{2.5}$ component in Al-free bridgmanite.

Fe^{3+} substitution predominantly follows the oxygen vacancy mechanism in $(\text{Mg,Fe})\text{O}$ -saturated Al-free bridgmanite when Fe^{3+} content is low.

The solubility of the $\text{MgFeO}_{2.5}$ component in Al-free bridgmanite is about 0.025 pfu, and relatively insensitive to temperature.

1. Introduction

Bridgmanite, with typical chemical formula $(\text{Mg,Fe})\text{SiO}_3$, comprises around 80 vol.% of the lower mantle (e.g. Frost, 2008; Ringwood, 1991; Tschauner et al., 2014), and therefore it dominates the physical and chemical processes of the lower mantle. Due to its variable valence, iron is the most important element that affects the properties of bridgmanite and thus mantle dynamics (e.g. Ismailova et al., 2016). Generally, iron is incorporated into the crystal structure of bridgmanite in the Mg site (A site) with the ferrous valence state. However, it is also known that a large amount of iron in bridgmanite can be in the ferric valence state even under reduced lower mantle conditions (Frost et al., 2004; Frost and McCammon, 2008; Grocholski et al., 2009; Jackson et al., 2005; Lauterbach et al., 2000; McCammon, 1997; McCammon et al., 2004). By analogy with aluminum substitutions in bridgmanite through the formation of $\text{MgAlO}_{2.5}$ and AlAlO_3 components (Brodholt, 2000; Kojitani et al., 2007; Liu et al., 2017a; 2017b; 2019a; 2019b; Navrotsky, 1999), it is expected that the $\text{MgFeO}_{2.5}$ (oxygen vacancy mechanism) and FeFeO_3 (charge-coupled mechanism) components, respectively, will be formed by Fe^{3+} incorporation through the following reactions (e.g. Hummer and Fei, 2012; Navrotsky, 1999),



where the subscripts A and B denote the Mg and Si sites, respectively (we follow the Kröger and Vink (1956) notation for point defects, i.e., $V_O^{\bullet\bullet}$ indicates a vacant O site with two effective positive charges, Mg_A^\times means a Mg ion on the A site with neutral charge, and Fe_B' represents an Fe^{3+} ion on the B site with one effective negative charge).

A question is how much Fe^{3+} in bridgmanite can be stored as $MgFeO_{2.5}$ and/or $FeFeO_3$ components under lower mantle conditions. The $MgAlO_{2.5}$ component in bridgmanite can reach up to 6.4 mol.% in the $MgO-SiO_2-Al_2O_3$ system depending on pressure, temperature, and Mg/Si atomic ratio, which is expected to significantly affect lower mantle rheology (Liu et al., 2017; 2019a; 2019b). In the case of the $MgO-SiO_2-Fe_2O_3$ system, although previous studies show that the Fe^{3+} occupies the A and B sites nearly equally (Catalli et al., 2010; Andrault and Bolfan-Casanova, 2001), indicating a very small amount of the $MgAlO_{2.5}$ component, their experiments were performed within diamond anvil cells where determination of sample chemical compositions are difficult, prohibiting a precise determination of $MgFeO_{2.5}$ and $FeFeO_3$ concentrations. Hummer and Fei (2012) investigated Fe^{3+} substitution mechanisms using multi-anvil experiments, however, their experiments did not reach chemical equilibrium as demonstrated by the coexistence of unreacted MgO and SiO_2 phases. Essentially, previous studies (Andrault and Bolfan-Casanova, 2001; Catalli et al., 2010; Hummer and Fei, 2012; Liu et al., 2018; Sinmyo et al., 2019) used starting materials without saturation of MgO (atomic Mg/Si = 1.0 or lower), which may prohibit the formation of $MgFeO_{2.5}$ based on observations that $MgAlO_{2.5}$ decreases with decreasing Mg/Si ratio in the $MgO-SiO_2-Al_2O_3$ system because of the reaction $2MgO + Al_2O_3 = 2MgAlO_{2.5}$ (Liu et al., 2019b). In contrast, the Earth's lower mantle contains ferropericlase, and the concentration of $MgFeO_{2.5}$ should thus be maximized.

Therefore, the phase relations of bridgmanite with $\text{MgFeO}_{2.5}$ and FeFeO_3 components, characterized by B-site Fe^{3+} , may depend on whether periclase (or ferropericlase) coexists or not according to the reaction $2\text{MgO} + \text{Fe}_2\text{O}_3 = 2\text{MgFeO}_{2.5}$. To clarify this further, we investigated the defect chemistry of bridgmanite in assemblage with a separate MgFe_2O_4 phase and either presence or absence of a (Mg,Fe)O phase, using a multi-anvil apparatus.

2. Experimental and analytical methods

2.1 Starting material and high-pressure experiments

MgO , SiO_2 , and Fe_2O_3 (purity > 99.9 %, natural isotopic ratios) from Sigma-Aldrich Corporation were used as starting materials. MgO and SiO_2 were dried at 1273 K, whereas Fe_2O_3 was dried at 773 K prior to weighing. Fine-mixed powders with bulk compositions of $\text{MgSiO}_3 + \text{MgFe}_2\text{O}_4 + \text{MgO}$ (60:20:20 in mole proportion, hereafter MgO-rich sample) and $\text{MgSiO}_3 + \text{MgFe}_2\text{O}_4 + \text{Fe}_2\text{O}_3$ (60:20:20 in mole proportion, hereafter Fe_2O_3 -rich sample) were obtained by repeatedly grinding in ethanol for homogeneity.

After drying in a vacuum furnace at 420 K, the two mixtures (both MgO-rich and Fe_2O_3 -rich separated by a piece of Pt foil) were filled into Pt tube capsules (OD = 1.0 mm, ID = 0.8 mm). Each capsule was loaded into an MgO sleeve within a LaCrO_3 heater in a 5 wt% Cr_2O_3 -doped MgO octahedron with an edge length of 7.0 mm (the standard 7/3 cell assembly at Bayerisches Geoinstitut), and compressed to 27 GPa at ambient temperature by eight pieces of Fujillooy-TF05 type tungsten carbide anvils with edge length of 26 mm and truncation edge length of 3.0 mm using the multi-anvil press at Bayerisches Geoinstitut, IRIS-15 (Ishii et al., 2016). After reaching the

target pressure of 27 GPa, the assembly was heated to a target temperature (1700-2300 K as listed in Table 1) at a ramping rate of 100 K/min measured by a W/Re (D-type) thermocouple. The annealing durations were 9 - 40 hours (Table 1), which is sufficiently long to achieve chemical equilibrium (Frost and Langenhorst, 2002) as confirmed by the run products. The samples were quenched to room temperature by switching off the heating power and decompressed to ambient conditions over a duration exceeding 15 hours. The recovered run products were mounted in epoxy resin and their cross sections were prepared by polishing with emery papers and diamond pastes.

2.2 Sample characterization

Scanning electron microscope (SEM): SEM analysis was performed on each sample, using a backscattering detector (BSE) and an acceleration voltage of 20 kV associated with an energy dispersive detector (EDS). Run products appeared as coexisting bridgmanite + MgFe_2O_4 + (Mg,Fe)O and bridgmanite + MgFe_2O_4 for the MgO-rich and Fe_2O_3 -rich samples, respectively (Table 1), as observed in BSE images (Fig. 1) and SEM-EDS point analysis. No unreacted particles (SiO_2 or Fe_2O_3 grains) were found in any of the sample capsules.

Microfocus X-ray diffraction (XRD): XRD analysis was performed on the recovered samples using a micro focused X-ray diffractometer (Bruker AXS D8 Discover) equipped with a two-dimensional solid-state detector and a micro focus source of Co-K α radiation operated at 40 kV and 500 μA . The exposure time is about 4 hours for each sample with beam size of $\sim 100 \mu\text{m}$. Bridgmanite and ferropericlase phases were clearly identified, and additional peaks were characterized as a CaMn_2O_4 -structured MgFe_2O_4 phase. This is consistent with the observation by Andrault and

Bolfan-Casanova (2001), although a CaTi_2O_4 -type structure was proposed by a more recent study (Greenberg et al., 2017). Pt peaks from sample capsules also appeared in the sample diffraction patterns due to the limited spatial resolution of the diffractometer (Fig. 2).

Mössbauer spectroscopy (MSS): Mössbauer spectra were collected over 500 μm diameter spots on samples of 120 μm thickness at room temperature in transmission mode on a constant acceleration Mössbauer spectrometer with a nominal 370 MBq ^{57}Co high-specific activity (point) source in a 12 μm Rh matrix. The velocity scale was calibrated relative to 25 μm thick α -Fe foil using the positions certified for standard reference material no. 1541 of the (former) National Bureau of Standards. Line widths of 0.36 mm/s for the outer lines of α -Fe were obtained at room temperature. Measurement times for each spectrum varied from 4 to 8 hours. The effective Mössbauer thickness of samples varied between 5 and 10 mg Fe/cm². Spectra were fit by the program MossA (Prescher et al., 2012) using the full transmission integral to multiple doublets with pseudo-Voigt line shape to account for next-nearest neighbor effects. There is no detectable Fe^{2+} in bridgmanite from the run products within experimental uncertainty (Fig. 3), and we assume that $\text{Fe}^{3+}/\Sigma\text{Fe} \approx 100\%$.

Electron probe microanalysis (EPMA): Concentrations of major elements (Mg, Si, Fe) in run products were obtained using a JEOL JXA-8200 electron microprobe with a wavelength-dispersive spectrometer (WDS) operated with an acceleration voltage of 15 kV, a beam current of 5 nA, and a counting time of 20 s. Focused point analysis with an excitation region of $\sim 1 \mu\text{m}$ was applied. An enstatite single crystal was used as the standard for Mg and Si, metallic Fe was used for Fe, whereas O was calculated by stoichiometry. Since the Pt capsule may absorb Fe from the samples, grains near the capsule wall (within a few microns) with slightly lower Fe% were avoided. The compositions of bridgmanite are listed in Table 1, whereas (Mg,Fe)O and MgFe_2O_4 phases, which

have Fe/Mg ratios of 0.02-0.07 and 1.94-2.38, respectively, are given in the online Supporting Information.

Molar concentrations of MgSiO_3 , $\text{MgFeO}_{2.5}$ and FeFeO_3 components in bridgmanite were calculated from:

$$\text{Mg}_x\text{Fe}_y\text{Si}_z\text{O}_{x+1.5y+2z} = z\text{MgSiO}_3 + (x - z)\text{MgFeO}_{2.5} + \frac{y-x+z}{2}\text{FeFeO}_3 \quad (3)$$

where x , y , and z are the atomic numbers per formula unit (pfu) from EPMA analysis. The $\text{Fe}^{2+}\text{SiO}_3$ component was excluded since $\text{Fe}^{3+}/\Sigma\text{Fe} \approx 100\%$ based on Mössbauer spectroscopy analysis, which is also confirmed by the low Fe/Mg ratio in ferropericlase.

3. Results and discussion

3.1. Total Fe^{3+} concentration in bridgmanite

The concentration of Fe^{3+} in bridgmanite systematically increases from 0.06 to 0.17 pfu and from 0.12 to 0.37 pfu in MgO-rich and Fe_2O_3 -rich samples, respectively, with increasing temperature from 1700 to 2300 K (Fig. 4a). It is noted that only two phases, bridgmanite and MgFe_2O_4 , coexist in run products of Fe_2O_3 -rich samples (Table 1). According to the phase rule, there is one more degree of freedom in addition to pressure and temperature in the MgO-SiO₂-Fe₂O₃ three-component system, and as a result, the Fe^{3+} concentration in bridgmanite should be correlated with the bulk Fe_2O_3 content in the starting material.

In contrast, three phases, bridgmanite, (Mg, Fe)O, and MgFe_2O_4 , coexist in the MgO-rich samples (Table 1). With fixed pressure and temperature, the composition of each phase should also be fixed

and independent of the bulk composition of the starting material in the three-component system. Therefore, the Fe^{3+} contents in the MgO-rich samples should represent the solubility of Fe^{3+} in bridgmanite with saturation of (Mg,Fe)O under the given pressure and temperature conditions, i.e., from 0.06 to 0.17 pfu with temperatures from 1700 to 2300 K (Fig. 4a).

3.2. $\text{MgFeO}_{2.5}$ and FeFeO_3 concentrations in bridgmanite by EPMA

The molar fractions of the bridgmanite components, MgSiO_3 , $\text{MgFeO}_{2.5}$, and FeFeO_3 were calculated sequentially based on Si, remaining Mg, and remaining Fe, respectively (Table 1). Fig. 4b illustrates the proportions of ferric iron components versus temperature and shows that the FeFeO_3 component increases systematically for both MgO-rich and Fe_2O_3 -rich samples with increasing temperature from 1700 to 2300 K. Bridgmanite in MgO-rich samples has lower proportions of the FeFeO_3 component than in Fe_2O_3 -rich samples.

The concentration of bridgmanite component $\text{MgFeO}_{2.5}$ is well below 2 mol% in Fe_2O_3 -rich samples although the uncertainty is relatively large. MgO-rich samples have a $\text{MgFeO}_{2.5}$ concentration of 2 to 3 mol.% at 1700-2300 K (Fig. 4b). Therefore, the presence of MgO enhances the formation of the $\text{MgFeO}_{2.5}$ component in bridgmanite, but only slightly in the presence of MgFe_2O_4 . A similar relationship was also observed in the Fe-free and Al-bearing bridgmanite coexisting with MgO and MgAl_2O_4 (Liu et al., 2019b). In contrast to the temperature-induced increase in the FeFeO_3 component, the concentration of the $\text{MgFeO}_{2.5}$ component is insensitive to temperature. This could be because either the temperature dependence is hidden by the uncertainty of data points, or because the $\text{MgFeO}_{2.5}$ reaches the maximum solubility even at 1700 K. Thus, the increase of total

Fe³⁺ with temperature is dominated by increasing FeFeO₃ component, rather than increasing MgFeO_{2.5} component.

3.3. Fe³⁺ substitution mechanisms in bridgmanite

It has been previously proposed that oxygen vacancy substitution by Fe³⁺ operates in bridgmanite in addition to the charge-coupled substitution mechanism (e.g. Frost and Langenhorst, 2002; Walter et al., 2004; Frost and McCammon, 2008), however, the concentration and formation condition of the MgFeO_{2.5} component have not been well constrained. Andrault and Bolfan-Casanova (2001) and Catalli et al. (2011) found roughly equal distribution of Fe³⁺ on Mg and Si sites, nevertheless, sample compositions in these diamond anvil experiments were uncertain due to small sample size. Hummer and Fei (2012) investigated Fe³⁺ substitution mechanisms based on well-constrained chemical compositions of bridgmanite samples recovered from large-volume multi-anvil experiments. They concluded that Fe³⁺ substitutes into bridgmanite by a combination of oxygen vacancy (Eq. 1) and charge-coupled (Eq. 2) mechanisms when Fe content is low (<0.05 pfu) because Mg content is either higher or comparable with Si. When Fe content is higher (0.074 pfu), charge-coupled (Eq. 2) and Mg vacancy mechanisms ($3\text{Mg}_A^{\times} \rightarrow 2\text{Fe}_A^{\bullet} + V_A''$ with Fe³⁺SiO₃ component) occur because Si > Mg. However, the relative magnitudes of Mg and Si that they obtained show no systematic variation with Fe content [Fig. 5 in this study and Fig. 3 in Hummer and Fei (2012)], and therefore are insufficient for interpretation of Fe³⁺ substitution mechanisms.

In our MgO-rich samples, both Mg and Si contents deviate slightly from theoretical calculations of a pure charge-coupled substitution mechanism (Fig. 5). The Mg content is systematically higher than Si within the investigated Fe content range from 0.06 to 0.17 pfu (Fig. 6), indicating an oxygen

vacancy substitution with formation of a $\text{MgFeO}_{2.5}$ component. On the other hand, Fe_2O_3 -rich samples have Mg and Si contents that match a pure charge-coupled mechanism without detectable oxygen vacancy substitution (Fig. 5). Therefore, the Fe^{3+} substitution mechanism in bridgmanite is dominantly controlled by the saturation condition of MgO, rather than by Fe content. The Mg vacancy substitution mechanism proposed by Hummer and Fei (2012) is not observed in this study, although the exact reason for this discrepancy is unclear. One possible reason is that ferric iron in their iron-rich sample ($\text{Fe} = 0.074$ pfu) might be partially reduced, leading to the formation of a $\text{Fe}^{2+}\text{SiO}_3$ component.

In Fig. 5, the lines of decreasing Mg and Si with increasing Fe^{3+} in bridgmanite from MgO-rich samples intersect the corresponding Si- and Mg-vectors for pure $\text{MgFeO}_{2.5}$ substitution at about 0.025 pfu, suggesting that oxygen vacancy substitution is preferred relative to charge-coupled substitution for low Fe^{3+} . When $\text{Fe}^{3+} \leq 0.025$ pfu, the majority of Fe^{3+} should follow the oxygen vacancy substitution mechanism. With increasing Fe^{3+} , $\text{MgFeO}_{2.5}$ content increases in this compositional range. When the $\text{MgFeO}_{2.5}$ content reaches the solubility limit of 0.025 pfu, additional Fe^{3+} will follow the charge-coupled mechanism and thus the amount of $\text{MgFeO}_{2.5}$ remains constant, which appears as nearly parallel curves of Mg or Si contents and pure charge-coupled substitution in Fig. 5.

3.4. Implications for bridgmanite chemistry

The Earth's lower mantle is mainly composed of bridgmanite, ferropericlase, and CaSiO_3 perovskite (Frost, 2008; Ringwood, 1991 Tschauner et al., 2014), meaning that bridgmanite is under MgO-saturated conditions. Since a significant amount of iron in bridgmanite is ferric (Frost et al., 2004;

Grocholski et al., 2009; Jackson et al., 2005; Lauterbach et al., 2000; McCammon, 1997; McCammon et al., 2004), the concentration of the $\text{MgFeO}_{2.5}$ component by oxygen vacancy substitution could be significant. On the other hand, bridgmanite in the lower mantle contains some Al (e.g. Irifune et al., 2010), which could affect the Fe^{3+} substitution mechanism via the formation of the FeAlO_3 component with Fe^{3+} and Al^{3+} occupying A and B sites, respectively (e.g. Richmond and Brodholt 1998; Zhang and Oganov 2006 as reviewed in Frost and McCammon, 2008). Similarly, Fe^{3+} may also affect formation of the $\text{MgAlO}_{2.5}$ component. The Al/Fe^{3+} ratio in Al-bearing bridgmanite under lower mantle conditions is generally larger than 1.0 in both peridotitic and basaltic lithologies (e.g., Mohn and Trønnes, 2016; Nakajima et al., 2012; Prescher et al., 2014), the FeAlO_3 component may thus prohibit oxygen-vacancy substitution, although some regions such as harzburgite layers that brought into the lower mantle by subduction have Al/Fe^{3+} ratios smaller than 1.0 (Liu et al., 2018). Studies of iron spin state indicate almost no Fe^{3+} (<1%) in the B-site because the spin transition for B-site Fe^{3+} is observed in Al-free bridgmanite at ~40-60 GPa, but not found in Al-bearing samples (e.g., Liu et al., 2018; Mohn and Trønnes, 2016). Nevertheless, oxygen vacancy substitution is significantly suppressed by pressure (Liu et al., 2017b), therefore, it is still unclear how much of the oxygen vacancy component is formed in Al-bearing bridgmanite, especially near the topmost lower mantle. Further studies at ~24-40 GPa in the $\text{MgO-SiO}_2\text{-Al}_2\text{O}_3\text{-Fe}_2\text{O}_3$ system are required.

Acknowledgments:

We appreciate the help of H. Fischer for high-pressure cell assembly machining, D. Krauß for assistance with EPMA analysis, R. Njul for sample preparation, and R. Huang for discussion.

Comments from R.G. Trønnes and an anonymous reviewer improved the manuscript. This work is funded by the Deutsche Forschungsgemeinschaft (DFG) (KA3434/3-1, KA3434/7-1, KA3434/8-1, KA3434/9-1, KA3434/12-1), the European Research Council (ERC) under the European Union's Horizon 2020 research and innovation program (Proposal No. 787 527), and the Bayerisches Geoinstitut visiting scientist program. The data sets for this research are given in Zenodo, doi: 10.5281/zenodo.3677121.

References:

- Andrault, D., Bolfan-Casanova, N. (2001). High-pressure phase transformations in the MgFe_2O_4 and Fe_2O_3 - MgSiO_3 systems. *Phys. Chem. Miner.* 28, 211-217.
- Brodholt, J.P. (2000). Pressure-induced changes in the compression mechanism of aluminous perovskite in the Earth's mantle. *Nature* 407, 620-622.
- Catalli, K., Shim, S.H., Prakapenka, V.B., Zhao, J., Sturhahn, W., Chow, P., Xiao, Y., Liu, H., Cynn, H., Evans, W.J. (2010). Spin state of ferric iron in MgSiO_3 perovskite and its effect on elastic properties. *Earth Planet. Sci. Lett.* 289, 68-75.
- Frost, D., Langenhorst, F. (2002). The effect of Al_2O_3 on Fe-Mg partitioning between magnesiowüstite and silicate perovskite. *Earth Planet. Sci. Lett.* 199, 227-241.
- Frost, D., Liebske, C., Langenhorst, F., McCammon, C.A., Trønnes, R.G., Rubie, D.C. (2004). Experimental evidence for the existence of iron-rich metal in the Earth's lower mantle. *Nature* 428, 409-412.

- Frost, D. (2008). The upper mantle and transition zone. *Elements* 4, 171-176.
- Frost, D., McCammon, C.A. (2008). The redox state of Earth's mantle. *Annu. Rev. Earth Planet. Sci.* 36, 389-420.
- Greenberg, E., Xu, W.M., Nikolaevsky, M., Bykova, E., Garbarino, G., Glazyrin, K., Merkel, D.G., Dubrovinsky, L., Pasternak, M.P., Rozenberg, G.K. (2017). High-pressure magnetic, electronic, and structural properties of $M\text{Fe}_2\text{O}_4$ ($M = \text{Mg}, \text{Zn}, \text{Fe}$) ferric spinels. *Phys. Rev. B* 95, 195150. Doi: 10.1103/PhysRevB.95.195150.
- Grocholski, B., Shim, S.H., Sturhahn, W., Zhao, J., Xiao, Y., Chow, P.C. (2009). Spin and valence states of iron in $(\text{Mg}_{0.8}\text{Fe}_{0.2})\text{SiO}_3$ perovskite. *Geophys. Res. Lett.* 36, L24303. Doi:10.1029/2009GL041262.
- Hirsch, L.M., Shankland, T.J. (1991). Point defects in $(\text{Mg}, \text{Fe})\text{SiO}_3$ perovskite. *Geophys. Res. Lett.* 18, 1305-1308.
- Hummer, D.R., Fei, Y. (2012). Synthesis and crystal chemistry of Fe^{3+} -bearing $(\text{Mg}, \text{Fe}^{3+})(\text{Si}, \text{Fe}^{3+})\text{O}_3$ perovskite. *Am. Miner.* 97, 1915-1921.
- Ishii, T., Shi, L., Huang, R., Tsujino, N., Druzhbin, D., Myhill, R., Li, Y., Wang, L., Yamamoto, T., Miyajima, N., Kawazoe, T., Nishiyama, N., Higo, Y., Tange, Y., Katsura, T. (2016). Generation of pressures over 40 GPa using Kawai-type multi-anvil press with tungsten carbide anvils. *Rev. Sci. Instr.* 87, 024501, doi: 10.1063/1.4941716.
- Ismailova, L., Bykova, E., Bykov, M., Cerantola, V., McCammon, C., Boffa-Ballaran, T., Bobrov, A., Sinmyo, R., Dubrovinskaia, N., Glazyrin, K., Liermann, H.P., Kuppenko, I., Hanfland, M., Prescher,

C., Prakapenka, V., Svitlyk, V., Dubrovinsky, L. (2006). Stability of Fe, Al-bearing bridgmanite in the lower mantle and synthesis of pure Fe-bridgmanite. *Sci. Adv.* 2, e1600427. Doi: 10.1126/sciadv.1600427.

Irifune, T., Shinmei, T., McCammon, C.A., Miyajima, N., Rubie, D.C., Frost, D.J. (2010). Iron partitioning and density changes of pyrolite in Earth's lower mantle. *Science* 327, 193-195.

Jackson, J.M., Sturhahn, W., Shen, G., Zhao, J., Hu, M.Y., Errandonea, D., Bass, J.D., Fei, Y. (2005). A synchrotron Mössbauer spectroscopy study of (Mg,Fe)SiO₃ perovskite up to 120 GPa. *Am. Miner.* 90, 199-205.

Kojitani, H., Katsura, T., & Akaogi, M. (2007). Aluminum substitution mechanisms in perovskite-type MgSiO₃: an investigation by Rietveld analysis. *Phys. Chem. Miner.* 34, 257–267.

Kröger, F.A., & Vink, H.J. (1956). Relations between the concentrations of imperfections in crystalline solids. *Solid State Phys.* 3, 307-435.

Lauterbach, S., McCammon, C.A., van Aken, P., Langenhorst, F., Seifert, F. (2000). Mössbauer and ELNES spectroscopy of (Mg,Fe)(Si,Al)O₃ perovskite: a highly oxidised component of the lower mantle. *Contrib. Miner. Petrol.* 138, 17-26.

Liu, J., Dorfam, S.M., Zhu, F., Li, J., Wang, Y., Zhang, D., Xiao, Y., Bi, W., Alp, E.E. (2018). Valence and spin states of iron are invisible in Earth's lower mantle. *Nat. Comm.* 9, 1284.

Liu, Z., Nishi, M., Ishii, T., Fei, H., Miyajima, N., Boffa-Ballaran, T., Ohfuji, H., Sakai, T., Wang, L., Shcheka, S., Arimoto, T., Tange, Y., Higo, Y., Irifune, T., Katsura, T. (2017a). Phase relations in the

system-MgSiO₃-Al₂O₃ up to 2300 K at lower mantle pressures. *J. Geophys. Res.* 122, 10.1002/2017JB014579.

Liu, Z., Ishii, T., Katsura, T. (2017b). Rapid decrease of MgAlO_{2.5} component in bridgmanite with pressure. *Geochem. Perspect. Lett.* 5, 12-18.

Liu, Z., Akaogi, M., Katsura, T. (2019a). Increase of the oxygen vacancy component in bridgmanite with temperature. *Earth Planet. Sci. Lett.* 505, 141-151.

Liu, Z., Boffa-Ballaran, T., Huang, R., Frost, D., Katsura, T. (2019b). Strong correlation of oxygen vacancies in bridgmanite with Mg/Si ratio. *Earth Planet. Sci. Lett.* 523, 115697.

McCammon, C.A. (1997). Perovskite as a possible sink for ferric iron in the lower mantle. *Nature* 387, 694-696.

McCammon, C.A. (1998). The crystal chemistry of ferric iron in Mg_{0.05}Fe_{0.95}SiO₃ perovskite as determined by Mössbauer spectroscopy in the temperature range 80-293 K. *Phys. Chem. Miner.* 25, 292-300.

McCammon, C.A., Lauterbach, S., Seifert, F., Langenhorst, F., van Aken, P.A. (2004). Iron oxidation state in lower mantle mineral assemblages I. Empirical relations derived from high-pressure experiments. *Earth Planet. Sci. Lett.* 222, 435-449.

Mohn, C.E., Trønnes, R.G. (2016). Iron spin state and site distribution in FeAlO₃-bearing bridgmanite. *Earth Planet. Sci. Lett.* 440, 178-186.

- Nakajima, Y., Frost, D.J., Rubie, D.C. (2012). Ferrous iron partitioning between magnesium silicate perovskite and ferropericlase and the composition of perovskite in the Earth's lower mantle. *J. Geophys. Res.* 117, B08201.
- Navrotsky, A. (1999). A lesson from ceramics. *Science* 284, 1788-1789.
- Prescher, C., McCammon, C., Dubrovinsky, L. (2012). MossA: a program for analyzing energy-domain Mössbauer spectra from conventional and synchrotron sources. *J. Appl. Crystallograph.* 45, 329-331.
- Ringwood, A.E. (1991). Phase transformations and their bearing on the constitution and dynamics of the mantle. *Geochim. Cosmochim. Acta* 55, 2083-2110.
- Richmond, N.C., Brodholt, J.P. (1998). Calculated role of aluminium in the incorporation of ferric iron into magnesium silicate perovskite. *Am. Miner.* 83, 947-951.
- Sinmyo, R., Nakajima, Y., McCammon, C.A., Miyajima, N., Petitgirard, S., Myhill, R., Dubrovinsky, L., Frost, D.J. (2019). Effect of Fe³⁺ on phase relations in the lower mantle: implications for redox melting in stagnant slabs. *J. Geophys. Res.* In press. 10.1029/2019JB017704.
- Terasaki, H., Frost, D., Rubie, D.C., Langenhorst, F. (2007). Interconnectivity of Fe-O-S liquid in polycrystalline silicate perovskite at lower mantle conditions. *Phys. Earth Planet. Int.* 161, 170-176.
- Tschauner, O., Ma, C., Beckett, J.R., Prescher, C., Prakapenka, V.B., Rossman, G.R. (2014). Discovery of bridgmanite, the most abundant mineral in Earth, in a shocked meteorite. *Science* 346, 1100-1102.

Walter, M.J., Kubo, A., Yoshino, T., Brodholt, J., Koga, K.T., & Ohishi, Y. (2004). Phase relations and equation-of-state of aluminous Mg-silicate perovskite and implications for Earth's lower mantle. *Earth Planet. Sci. Lett.* 222, 501-516.

Zhang, F., Oganov, A.R. (2006). Valence state and spin transitions of iron in Earth's mantle silicates. *Earth Planet. Sci. Lett.* 249, 436-443.

Figure captions:

Fig. 1. Backscattered SEM images of run products at 27 GPa and 1700-2300 K for both MgO-rich and Fe₂O₃-rich samples, which appear as coexisting bridgmanite (grey) + MgFe₂O₄ (bright) + (Mg,Fe)O (dark) phases and bridgmanite (grey) + MgFe₂O₄ (bright) phases, respectively.

Fig. 2. Representative X-ray diffraction spectra of run products (run I567). Top: Fe₂O₃-rich sample. Bottom: MgO-rich sample. Bridgmanite (bdg), CaMn₂O₄-type MgFe₂O₄ (CM), and (Mg,Fe)O-periclase (pc) phases were identified, as well as the Pt from the sample capsules.

Fig. 3. Room temperature Mössbauer spectra of run products (Run I574). The blue and purple doublets correspond to Fe³⁺ in bridgmanite and MgFe₂O₄ phases, respectively, whereas the yellow doublet is assigned to Fe²⁺ in (Mg,Fe)O. There is no detectable Fe²⁺ in bridgmanite within the data scatter.

Fig. 4. Atomic concentrations of MgFeO_{2.5}, FeFeO₃, and total Fe³⁺ per formula unit (oxygen = 3) in bridgmanite, assuming MgFeO_{2.5} + FeFeO₃ + MgSiO₃ = 100 %. Upper panel: Total Fe³⁺ concentration. Lower panel: proportions of the MgFeO_{2.5} and FeFeO₃ components.

Fig. 5. Mg (open symbols) and Si (filled symbols) per formula unit in bridgmanite (oxygen = 3) as a function of the Fe^{3+} content for both MgO-rich and Fe_2O_3 -rich samples. Error bars represent one standard deviation of uncertainty calculated from EPMA measurements in Table 1. Small orange and dark blue symbols are from ref. HF12 (Hummer and Fei, 2012). Thin solid and dashed lines indicate theoretical concentrations of Mg, Si per formula unit by pure FeFeO_3 and $\text{MgFeO}_{2.5}$ substitutions, respectively. Crossovers of Mg, Si pfu in MgO-rich samples (red lines) and theoretical calculations of pure $\text{MgFeO}_{2.5}$ substitution (thin dashed lines) occur at $\text{Fe}^{3+} \approx 0.025$ pfu.

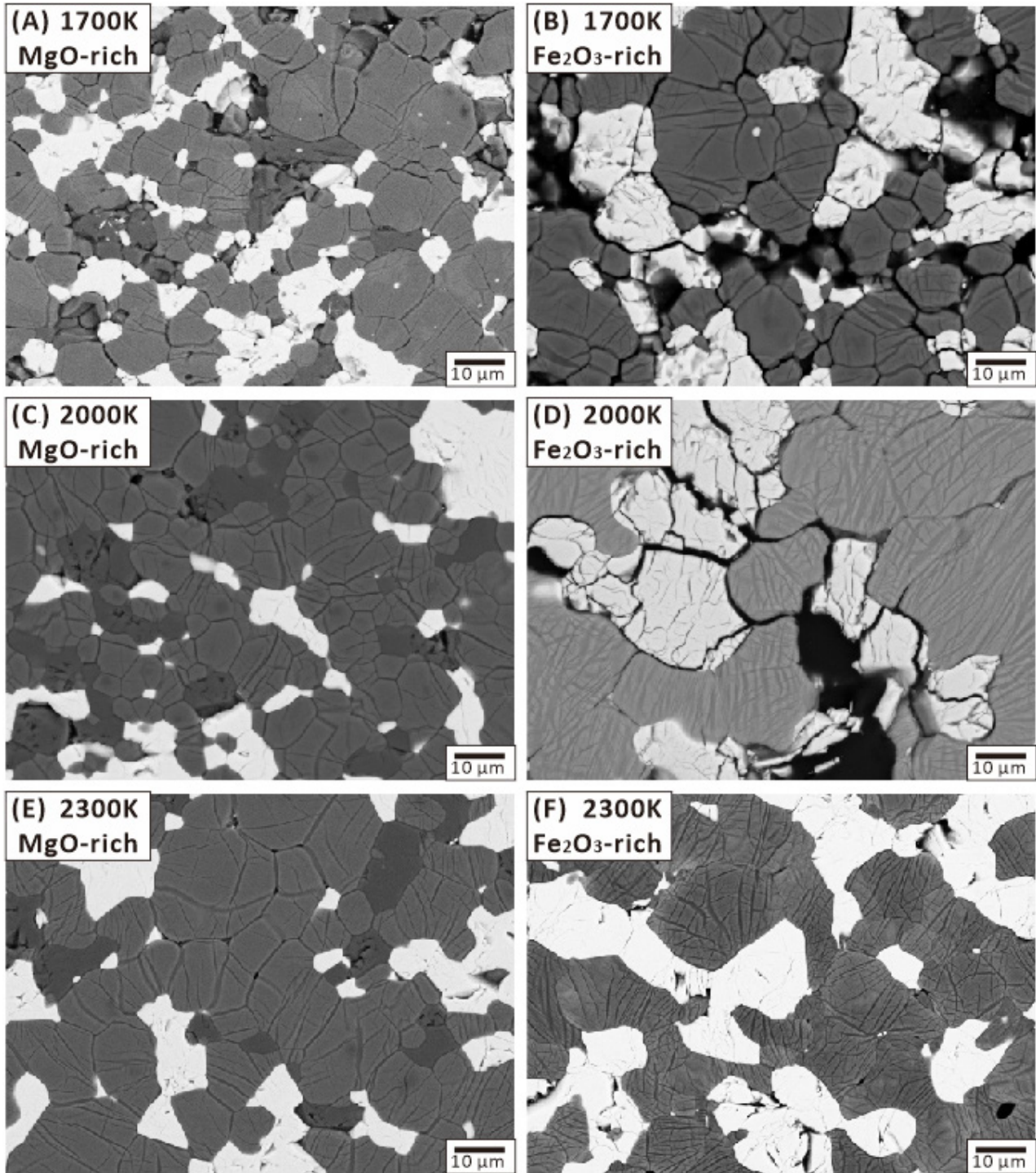
- 1 Table 1: Run conditions, phase assemblage, and composition of bridgmanite in run products. All experiments were performed at 27
 2 GPa. *T*: temperature. *t*: annealing duration. *N*: number of analyzed points by EPMA.

Starting material	Run No.	T (K)	<i>t</i> (h)	Phase assemblage	Composition of bridgmanite										
					N	MgO wt%	SiO ₂ wt%	Fe ₂ O ₃ wt%	Total wt%	Mg pfu	Si pfu	Fe pfu	O pfu	FeFeO ₃ mol%	MgFeO _{2.5} mol%
MgO-rich ^{*a}	I567	2000	24	Bridgmanite + MgFe ₂ O ₄ + (Mg,Fe)O	13	37.52 (67)	54.38 (96)	10.55 (109)	102.45 (54)	0.946 (10)	0.920 (11)	0.134 (15)	2.987 (8)	5.4 (10)	2.6 (15)
	I574	2300	9		17	35.94 (99)	52.29 (80)	13.47 (42)	101.70 (123)	0.923 (15)	0.902 (13)	0.175 (7)	2.989 (14)	7.6 (15)	2.2 (27)
	I580	1700	40		14	40.02 (0.37)	58.03 (0.38)	4.77 (0.34)	102.82 (0.54)	0.984 (6)	0.957 (6)	0.059 (4)	2.987 (6)	1.6 (7)	2.7 (12)
	I597	1700	40		8	39.83 (38)	58.16 (63)	4.90 (25)	102.88 (71)	0.980 (5)	0.960 (6)	0.061 (3)	2.990 (5)	2.0 (5)	2.0 (10)
Fe ₂ O ₃ -rich ^{*b}	I567	2000	24	Bridgmanite + MgFe ₂ O ₄	16	33.59 (80)	49.12 (118)	18.51 (106)	101.22 (92)	0.885 (14)	0.868 (14)	0.246 (16)	2.992 (12)	11.5 (14)	1.7 (23)
	I574	2300	9		15	29.72 (94)	43.57 (194)	26.67 (211)	99.96 (170)	0.821 (18)	0.807 (25)	0.372 (36)	2.993 (13)	17.9 (18)	1.4 (26)
	I597	1700	40		13	37.71 (69)	56.03 (88)	9.23 (135)	102.98 (63)	0.943 (11)	0.940 (10)	0.117 (18)	2.998 (6)	5.7 (11)	0.3 (11)
	I681	2000	10		12	32.78 (55)	49.34 (152)	18.74 (74)	100.85 (182)	0.870 (8)	0.879 (13)	0.251 (12)	3.004 (9)	13.0 (8)	-0.8 (18)
	I646	2300	20		9	31.45(94)	46.78(126)	23.40 (246)	101.63 (67)	0.843 (19)	0.841 (18)	0.316 (35)	2.999 (7)	15.7 (19)	0.2 (13)

3 ^{*a}: MgO-rich: mixture of oxides with bulk composition of MgSiO₃+MgFe₂O₄+MgO (60:20:20 atomic ratio).

4 ^{*b}: Fe₂O₃-rich: mixture of oxides with bulk composition of MgSiO₃+MgFe₂O₄+Fe₂O₃ (60:20:20 atomic ratio).

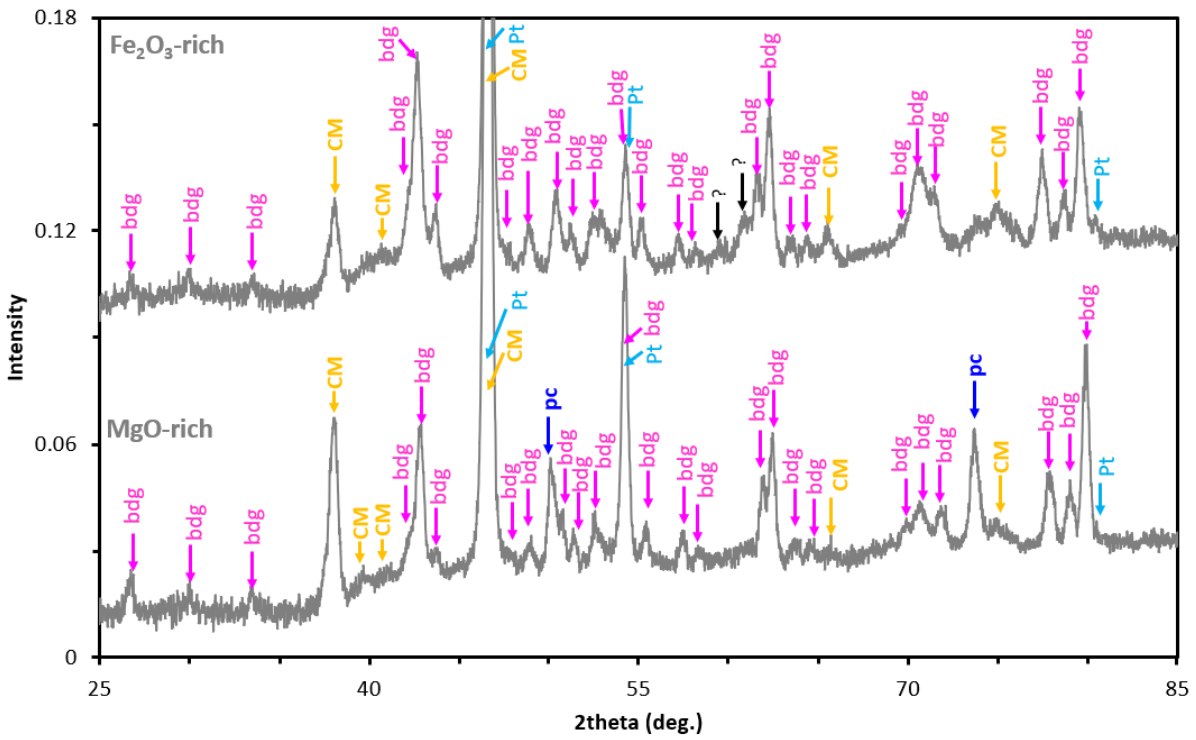
5



6

7

Fig. 1



8
9
10

Fig. 2

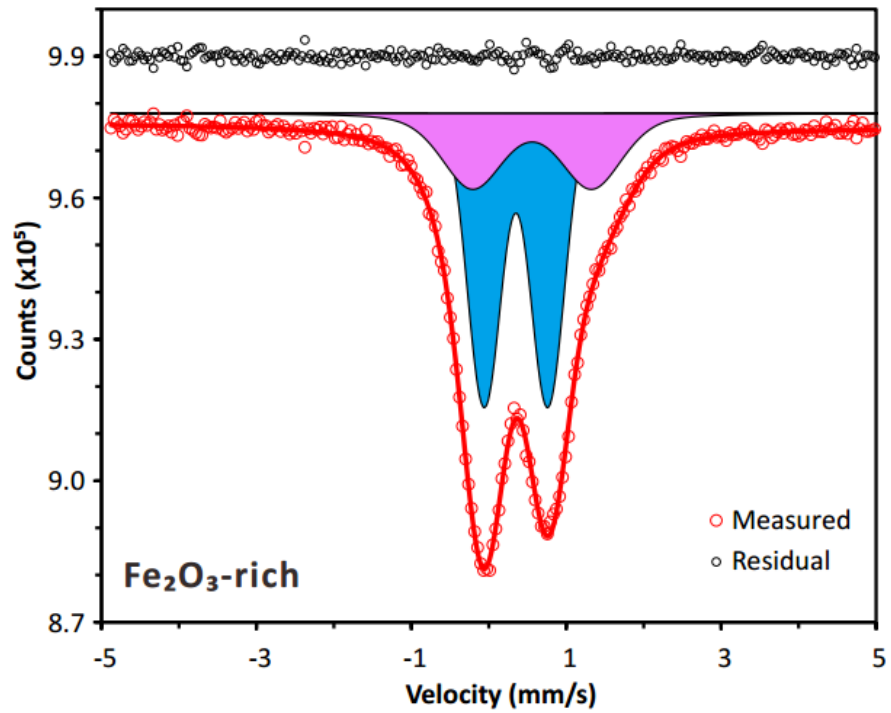
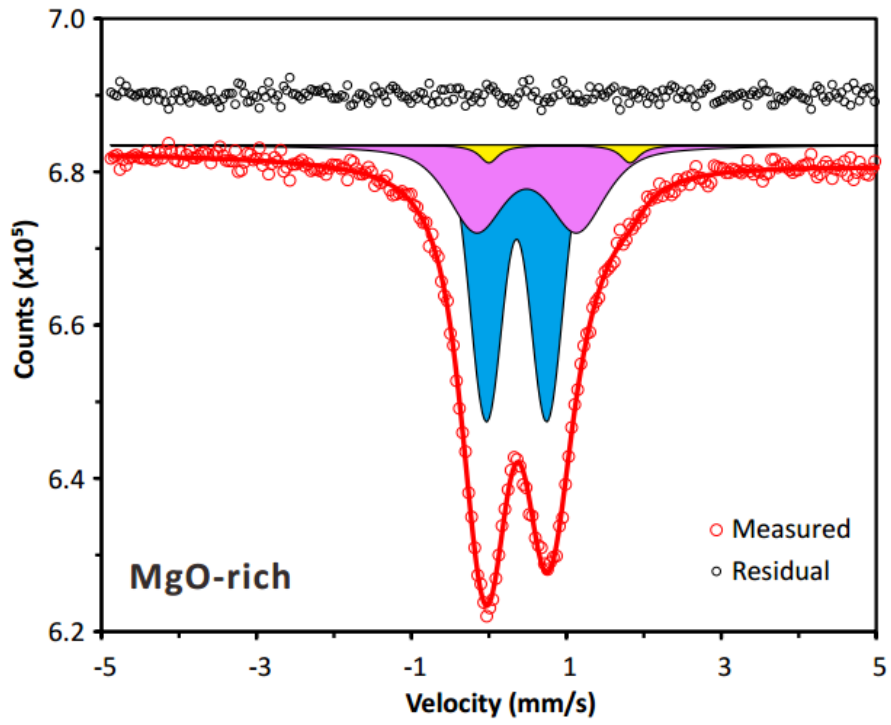
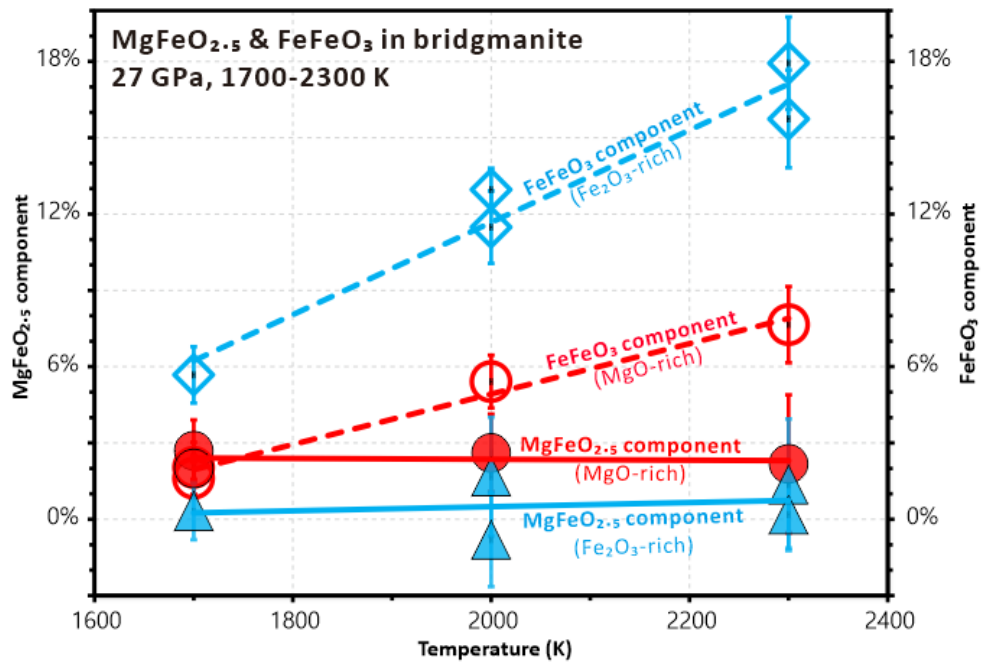
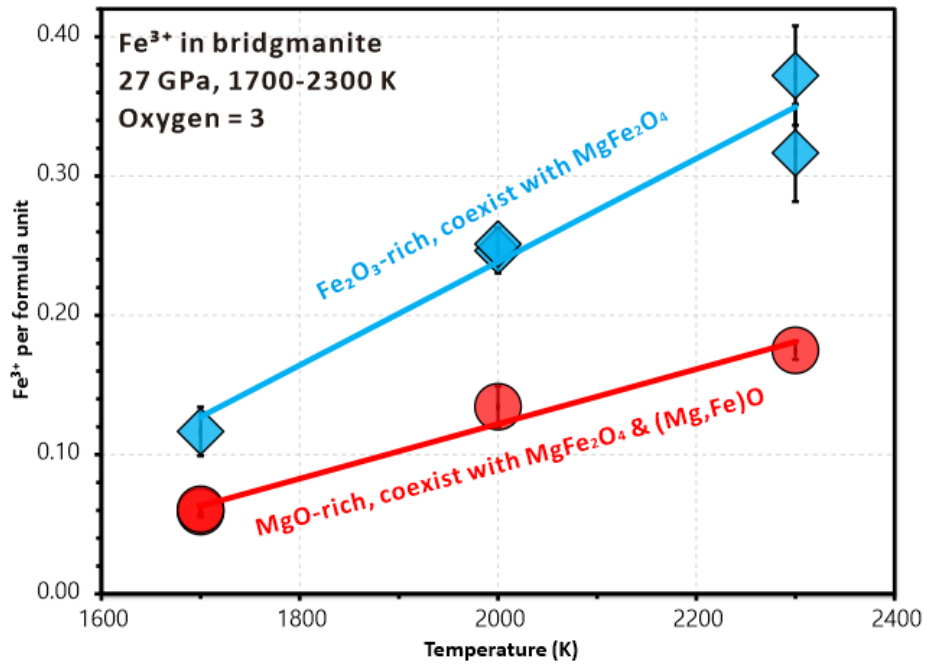


Fig. 3

11

12

13

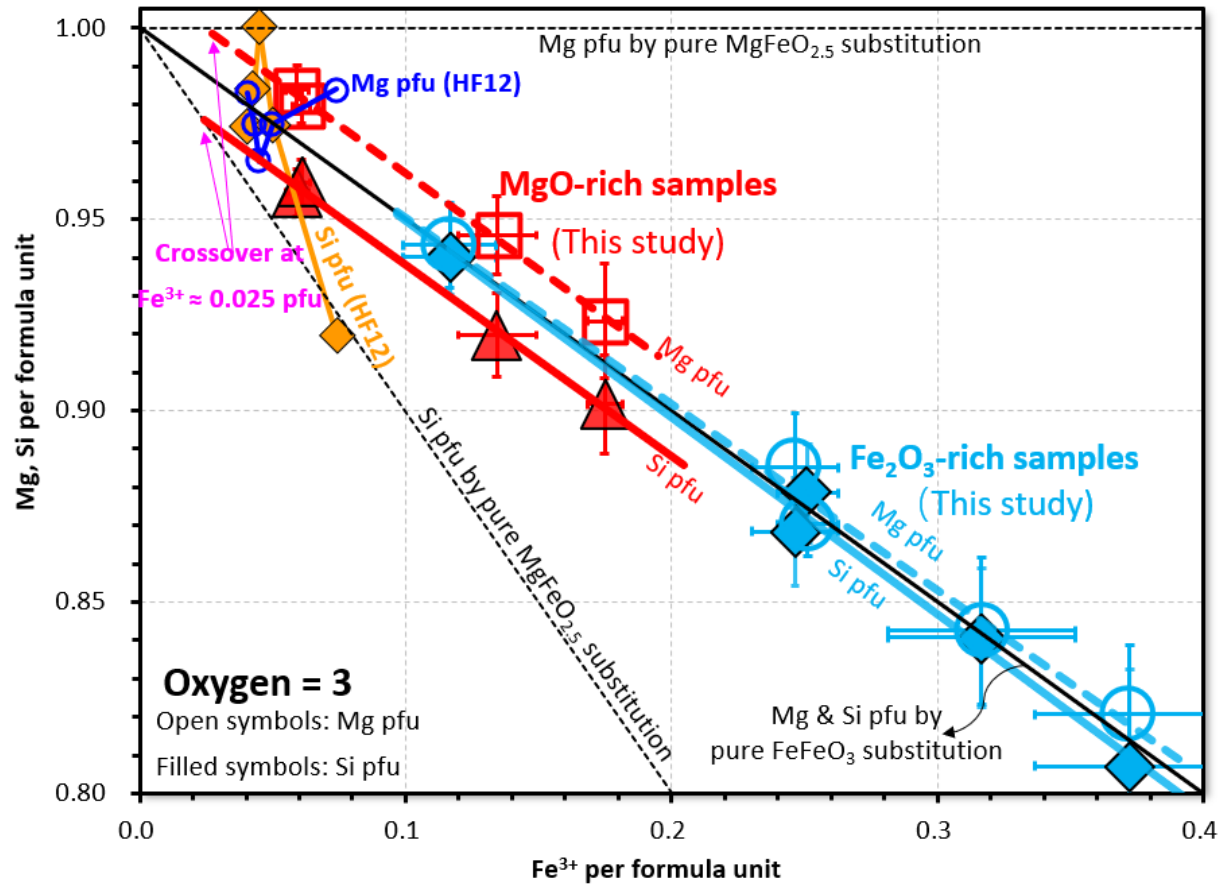


14

15

16

Fig. 4



17

18

Fig. 5